Research Article | Vol. 26, No. 18 | 3 Sep 2018 | OPTICS EXPRESS A865
Optics EXPRESS

Absorption enhancement in methylammonium lead iodide perovskite solar cells with embedded arrays of dielectric particles

ALBERTO JIMÉNEZ-SOLANO,[1,2] SOL CARRETERO-PALACIOS,[1] AND HERNÁN MÍGUEZ[1,*]

[1]*Multifunctional Optical Materials Group, Institute of Materials Science of Sevilla, Consejo Superior de Investigaciones Científicas, Universidad de Sevilla (CSIC-US), Américo Vespucio, 49, 41092, Sevilla, Spain*
[2]*Present address: Max Planck Institute for Solid State Research, Heisenbergstrasse 1, 70569 Stuttgart, Germany*
[*]*h.miguez@csic.es*

Abstract: In the field of hybrid organic-inorganic perovskite based photovoltaics, there is a growing interest in the exploration of novel and smarter ways to improve the cells light harvesting efficiency at targeted wavelength ranges within the minimum volume possible, as well as in the development of colored and/or semitransparent devices that could pave the way both to their architectonic integration and to their use in the flowering field of tandem solar cells. The work herein presented targets these different goals by means of the theoretical optimization of the optical design of standard opaque and semitransparent perovskite solar cells. In order to do so, we focus on the effect of harmless, compatible and commercially available dielectric inclusions within the absorbing material, methylammonium lead iodide (MAPI). Following a gradual and systematic process of analysis, we are capable of identifying the appearance of collective and hybrid (both localized and extended) photonic resonances which allow to significantly improve light harvesting and thus the overall efficiency of the standard device by above 10% with respect to the reference value while keeping the semiconductor film thickness to a minimum. We believe our results will be particularly relevant in the promising field of perovskite solar cell based tandem photovoltaic devices, which has posed new challenges to the solar energy community in order to maximize the performance of semitransparent cells, but also for applications focusing on architectonic integration.

OCIS codes: (350.6050) Solar energy; (220.0220) Optical design and fabrication.

References and links

1. M. M. Lee, J. Teuscher, T. Miyasaka, T. N. Murakami, and H. J. Snaith, "Efficient hybrid solar cells based on meso-superstructured organometal halide perovskites," Science **338**(6107), 643–647 (2012).
2. M. A. Green, A. Ho-Baillie, and H. J. Snaith, "The emergence of perovskite solar cells," Nat. Photonics **8**(7), 506–514 (2014).
3. S.-H. Bae, H. Zhao, Y.-T. Hsieh, L. Zuo, N. De Marco, Y. S. Rim, G. Li, and Y. Yang, "Printable Solar Cells from Advanced Solution-Processible Materials," Chem **1**(2), 197–219 (2016).
4. https://www.nrel.gov/pv/assets/images/efficiency-chart.png (accessed: July 11, 2018).
5. J. H. Noh, S. H. Im, J. H. Heo, T. N. Mandal, and S. I. Seok, "Chemical management for colorful, efficient, and stable inorganic-organic hybrid nanostructured solar cells," Nano Lett. **13**(4), 1764–1769 (2013).
6. W. Zhang, M. Anaya, G. Lozano, M. E. Calvo, M. B. Johnston, H. Míguez, and H. J. Snaith, "Highly efficient perovskite solar cells with tunable structural color," Nano Lett. **15**(3), 1698–1702 (2015).
7. G. E. Eperon, S. D. Stranks, C. Menelaou, M. B. Johnston, L. M. Herza, and H. J. Snaith, "Formamidinium lead trihalide: a broadly tunable perovskite for efficient planar heterojunction solar cells," Energy Environ. Sci. **7**(3), 982–988 (2014).
8. C. Roldan-Carmona, O. Malinkiewicz, R. Betancur, G. Longo, C. Momblona, F. Jaramillo, L. Camacho, and H. Bolink, "Flexible high efficiency perovskite solar cells," Energy Environ. Sci. **7**(3), 994–997 (2014).
9. J.-W. Lee, Y.-T. Hsieh, N. De Marco, S.-H. Bae, Q. Han, and Y. Yang, "Halide perovskites for tandem solar cells," J. Phys. Chem. Lett. **8**(9), 1999–2011 (2017).

#328769 https://doi.org/10.1364/OE.26.00A865
Journal © 2018 Received 1 May 2018; revised 8 Jul 2018; accepted 10 Jul 2018; published 21 Aug 2018

Optics EXPRESS

10. N. C. Jeong, C. Prasittichai, and J. T. Hupp, "Photocurrent enhancement by surface plasmon resonance of silver nanoparticles in highly porous dye-sensitized solar cells," Langmuir **27**(23), 14609–14614 (2011).
11. Z. Wang, H. Kawauchi, T. Kashima, and H. Arakawa, "Significant influence of TiO_2 photoelectrode morphology on the energy conversion efficiency of N719 dye-sensitized solar cell," Coord. Chem. Rev. **248**(13–14), 1381–1389 (2004).
12. O. K. Varghese, M. Paulose, and C. A. Grimes, "Long vertically aligned titania nanotubes on transparent conducting oxide for highly efficient solar cells," Nat. Nanotechnol. **4**(9), 592–597 (2009).
13. S. Jang, J. Yoon, K. Ha, M.-C. Kim, D. H. Kim, S. M. Kim, S. M. Kang, S. J. Park, H. S. Jung, and M. Choi, "Facile fabrication of three-dimensional TiO_2 structures for highly efficient perovskite solar cells," Nano Energy **22**, 499–506 (2016).
14. S. M. Kang, S. Jang, J.-K. Lee, J. Yoon, D.-E. Yoo, J.-W. Lee, M. Choi, and N.-G. Park, "Moth-Eye TiO2 Layer for Improving Light Harvesting Efficiency in Perovskite Solar Cells," Small **12**(18), 2443–2449 (2016).
15. J. Yin, H. Qu, J. Cao, H. Tai, J. Li, and N. Zheng, "Light absorption enhancement by embedding submicron scattering TiO_2 nanoparticles in perovskite solar cells," RSC Advances **6**(29), 24596–24602 (2016).
16. S. M. Kang, N. Ahn, J.-W. Lee, M. Choi, and N.-G. Park, "Water-Repellent Perovskite Solar Cell," J. Mater. Chem. A Mater. Energy Sustain. **2**(47), 20017–20021 (2014).
17. H.-L. Hsu, T.-Y. Juang, C.-P. Chen, C.-M. Hsieh, C.-C. Yang, C.-L. Huang, and R.-J. Jeng, "Enhanced efficiency of organic and perovskite photovoltaics from shape-dependent broadband plasmonic effects of silver nanoplates," Sol. Energy Mater. Sol. Cells **140**, 224–231 (2015).
18. R. S. Wu, B. C. Yang, C. J. Zhang, Y. L. Huang, Y. X. Cui, P. Liu, C. H. Zhou, Y. Y. Hao, Y. L. Gao, and J. L. Yang, "Prominent efficiency enhancement in perovskite solar cells employing silica-coated gold nanorods," J. Phys. Chem. C **120**(13), 6996–7004 (2016).
19. W. Zhang, M. Saliba, S. D. Stranks, Y. Sun, X. Shi, U. Wiesner, and H. J. Snaith, "Enhancement of perovskite-based solar cells employing core-shell metal nanoparticles," Nano Lett. **13**(9), 4505–4510 (2013).
20. Z. Lu, X. Pan, Y. Ma, Y. Li, L. Zheng, D. Zhang, Q. Xu, Z. Chen, S. Wang, B. Qu, F. Liu, Y. Huang, L. Xiao, and G. Qihuang, "Plasmonic-enhanced perovskite solar cells using alloy popcorn nanoparticles," RSC Advances **5** (15), 11175–11179 (2015).
21. S. Carretero-Palacios, M. E. Calvo, and H. Míguez, "Absorption enhancement in organic–inorganic halide perovskite films with embedded plasmonic gold nanoparticles," J Phys Chem C Nanomater Interfaces **119**(32), 18635–18640 (2015).
22. S. Carretero-Palacios, A. Jiménez-Solano, and H. Míguez, "Plasmonic nanoparticles as light-harvesting enhancers in perovskite solar cells: a user's guide," ACS Energy Lett. **1** (1), 323–331 (2016).
23. I. Rodriguez, L. Shi, X. Lu, B. A. Korgel, R. A. Álvarez-Puebla, and F. Meseguer, "Silicon nanoparticles as Raman scattering enhancers," Nanoscale **6**(11), 5666–5670 (2014).
24. U. Zywietz, A. B. Evlyukhin, C. Reinhardt, and B. N. Chichkov, "Laser printing of silicon nanoparticles with resonant optical electric and magnetic responses," Nat. Commun. **5**(1), 3402 (2014).
25. J. M. Miranda-Muñoz, S. Carretero-Palacios, A. Jiménez-Solano, Y. Li, G. Lozano, and H. Míguez, "Efficient bifacial dye-sensitized solar cells through disorder by design," J Mater Chem A Mater **4**(5), 1953–1961 (2016).
26. J. M. Miranda-Muñoz, G. Lozano, and H. Míguez, "Design and realization of a novel optically disordered material: a demonstration of a Mie glass," Adv. Opt. Mater. **5**(10), 1700025 (2017).
27. M. Anaya, G. Lozano, M. E. Calvo, W. Zhang, M. B. Johnston, H. J. Snaith, and H. Míguez, "Optical description of mesostructured organic–inorganic halide perovskite solar cells," J. Phys. Chem. Lett. **6**(1), 48–53 (2015).
28. L. Solutions, Inc. http://www.lumerical.com/tcad-products/fdtd/ (accessed: April 4, 2018).
29. J. P. Correa-Baena, M. Anaya, G. Lozano, W. Tress, K. Domanski, M. Saliba, T. Matsui, T. J. Jacobsson, M. E. Calvo, A. Abate, M. Grätzel, H. Míguez, and A. Hagfeldt, "Unbroken perovskite: interplay of morphology, electro-optical properties and ionic movement," Adv. Mater. **28**(25), 5031–5037 (2016).
30. P. Löper, M. Stuckelberger, B. Niesen, J. Werner, M. Filipič, S. J. Moon, J. H. Yum, M. Topič, S. De Wolf, and C. Ballif, "Complex refractive index spectra of $CH_3NH_3PbI_3$ perovskite thin films determined by spectroscopic ellipsometry and spectrophotometry," J. Phys. Chem. Lett. **6**(1), 66–71 (2015).
31. M. Anaya, G. Lozano, M. E. Calvo, and H. Míguez, "ABX_3 perovskites for tandem solar cells," Joule **1**(4), 769–793 (2017).
32. H. W. Deckman and J. H. Dunsmuir, "Natural lithography," Appl. Phys. Lett. **41**(4), 377–379 (1982).
33. A. van Blaaderen, R. Ruel, and P. Wiltzius, "Template-directed colloidal crystallization," Nature **385**(6614), 321–324 (1997).
34. P. Jiang, T. Prasad, M. J. McFarland, and V. L. Colvin, "Two-dimensional nonclose-packed colloidal crystals formed by spincoating," Appl. Phys. Lett. **89**(1), 011908 (2006).
35. R. Guerra, I. Marri, R. Magri, L. Martin-Samos, O. Pulci, E. Degoli, and S. Ossicini, "Optical properties of silicon nanocrystallites in SiO_2 matrix: crystalline vs. amorphous case," Superlattices Microstruct. **46**(1–2), 246–252 (2009).
36. S. Wippermann, M. Vörös, A. Gali, F. Gygi, G. T. Zimanyi, and G. Galli, "Solar nanocomposites with complementary charge extraction pathways for electrons and holes: Si embedded in ZnS," Phys. Rev. Lett. **112**(10), 106801 (2014).
37. E. Tiguntseva, A. Chebykin, A. Ishteev, R. Haroldson, B. Balachandran, E. Ushakova, F. Komissarenko, H. Wang, V. Milichko, A. Tsypkin, D. Zuev, W. Hu, S. Makarov, and A. Zakhidov, "Resonant silicon nanoparticles

Optics EXPRESS

for enhancement of light absorption and photoluminescence from hybrid perovskite films and metasurfaces," Nanoscale **9**(34), 12486–12493 (2017).
38. M. L. Petrus, J. Schlipf, C. Li, T. P. Gujar, N. Giesbrecht, P. Müller-Buschbaum, M. Thelakkat, T. Bein, S. Hüttner, and P. Docampo, "Capturing the Sun: A Review of the Challenges and Perspectives of Perovskite Solar Cells," Adv. Energy Mater. **7**(16), 1700264 (2017).
39. O. E. Semonin, G. A. Elbaz, D. B. Straus, T. D. Hull, D. W. Paley, A. M. van der Zande, J. C. Hone, I. Kymissis, C. R. Kagan, X. Roy, and J. S. Owen, "Limits of Carrier Diffusion in n-Type and p-Type CH3NH3PbI3 Perovskite Single Crystals," J. Phys. Chem. Lett. **7**(17), 3510–3518 (2016).
40. W. Tian, C. Zhao, J. Leng, R. Cui, and S. Jin, "Visualizing Carrier Diffusion in Individual Single-Crystal Organolead Halide Perovskite Nanowires and Nanoplates," J. Am. Chem. Soc. **137**(39), 12458–12461 (2015).
41. K. Handloser, N. Giesbrecht, T. Bein, P. Docampo, M. Handloser, and A. Hartschuh, "Contactless Visualization of Fast Charge Carrier Diffusion in Hybrid Halide Perovskite Thin Films," ACS Photonics **3**(2), 255–261 (2016).
42. A. Jiménez-Solano, J. F. Galisteo-López, and H. Míguez, "Absorption and Emission of Light in Optoelectronic Nanomaterials: The Role of the Local Optical Environment," J. Phys. Chem. Lett. **9**(8), 2077–2084 (2018).
43. R. L. Milot, G. E. Eperon, H. J. Snaith, M. B. Johnston, and L. M. Herz, "Temperature-Dependent Charge-Carrier Dynamics in $CH_3NH_3PbI_3$ Perovskite Thin Films," Adv. Funct. Mater. **25**(39), 6218–6227 (2015).

1. Introduction

Since the emergence of perovskite solar cells (PSC) as high efficient devices, the photovoltaic [1–3] field has undergone a revolution. The great capability of PSC for solar light absorption has given rise to devices displaying remarkable certified power-conversion efficiencies as high as 22.7% [4] in single junction configurations. In addition, the versatile optical designs and synthetic methods that might be applied to them, lend them with outstanding properties such as color tunability [5,6], transparency [7], or flexibility [8]. Moreover, tandem junction solar cells allow the improvement of the efficiency of photovoltaics by combining a semi-transparent perovskite-based solar cell with a variety of well-established photovoltaic devices such as organic, silicon, and $Cu(In,Ga)(S,Se)_2$ (CIGS) solar cells [9]. With the aim of maximizing light absorption in the red part of the visible solar spectrum (at which perovskite films absorb less neatly), while preserving both high efficiencies and thin enough perovskite films (in order to minimize their lead content), several approaches employing optical design and previously applied to other solution processed solar cells [10–12] have been proposed. Examples of these concepts include the addition of 3-dimensional (3D) nanopatterned mesoporous titanium dioxide (TiO_2) layers [13,14] at the interface between the substrate and the active layer, the dispersion of disordered TiO_2 particles [15], integrating bifunctional polydimethylsiloxane film [16] or metal [17–20] nanoparticles into the mesoporous scaffold, or the distribution of plasmonic nanoparticles directly embedded into the perovskite film [21,22]. However, no systematic studies on the outcome of the solar absorption in perovskite cells embedding dielectric or semiconductor particles have been shown up to now.

In this work, we present a theoretical analysis of the effect of the inclusion of arrays of dielectric spheres on the solar absorption of methylammonium lead iodide (MAPI) cells. We first consider simple schemes in which the particle arrays are located at the interface between a glass substrate and a MAPI film (Fig. 1(a)), while covered by a hole-transporting material, to identify the best performing dielectric material to maximize light collection in the MAPI film. Secondly, a full perovskite solar cell (Fig. 1(b)), either on an opaque or semi-transparent configuration, is analysed taking into account the optimum dielectric material attained in the simple schemes. Dielectric particle composition, shape, and size are selected among those experimentally available [23–26]. Also, the thicknesses of MAPI films considered are within the range typically employed in the field [27]. In particular, we consider SiO_2, TiO_2, and Si particles of radius r ranging from 80 nm to 140 nm, and array periods p spanning from 250 to 600 nm. In general, we take a simple arrangement in which a thin MAPI film of $h = 300$ nm thickness lies on top of a semi-infinite glass substrate while being coated by a hole-transporting material. Thicker MAPI films are also considered in specific cases for comparison. For the complete solar cell configuration, standard material thicknesses widely used in literature have been employed (as indicated in Fig. 1(b)).

Optics EXPRESS

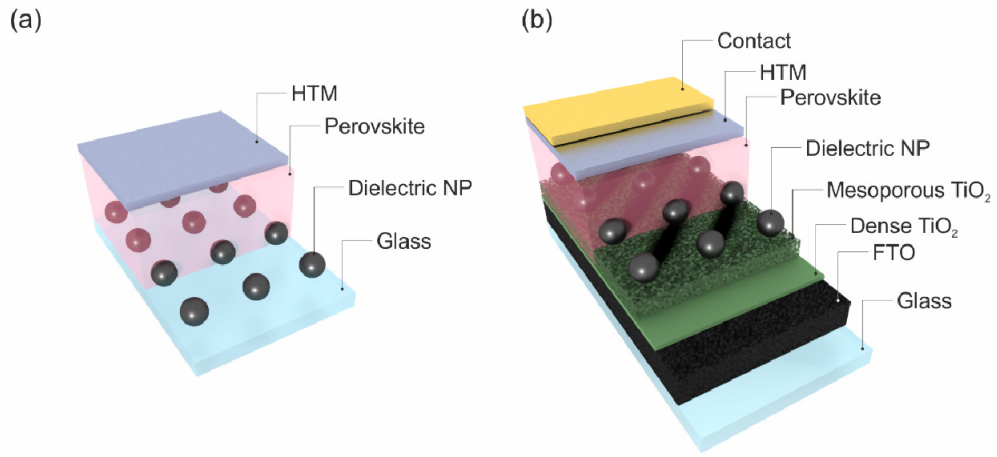

Fig. 1. (a) Schematics of the simple system under study: a particle array is placed at the interface between a glass substrate and a MAPI film, having a hole-transporting material (HTM) as a cover. The system is illuminated by a plane wave injected from the glass substrate. The particle size is defined by the radius, r, and the lattice parameters by the period, p. The MAPI film thickness is characterized by h. (b) Scheme of the architecture of the simulated device: glass substrate, 500 nm of FTO layer, 10 nm of TiO_2 compact layer, 100 nm of 50% porous TiO_2 scaffold fully infiltrated by perovskite, 300 nm of perovskite capping layer with array particles at the bottom surface, 80 nm of spiro-OMeTAD, and 80 nm of gold contact (for the standard cell) or 100 nm of ITO contact (for the semi-transparent cell).

2. Methods

The commercial software Lumerical Solutions Inc. (v8.17.1157) [28] is used for employing 3D Finite-Difference Time-Domain (FDTD) numerical simulations. In our simulations we consider a multilayer system in which each material (j) is characterized by a proper complex refractive index, $\tilde{n}_j(\lambda) = n_j(\lambda) + ik_j(\lambda)$, with λ being the incident wavelength. Specifically, in the simple film structure, we assume non absorbing materials for the substrate and the cover, with $\tilde{n}_g(\lambda) = 1.5$ and $\tilde{n}_s(\lambda) = 1.7$ (and $k_{SiO_2} = k_{TiO_2} = 0$), resembling those of glass and Spiro OMeTAD materials, respectively. For SiO_2 and TiO_2 particles we take $\tilde{n}_{SiO_2}(\lambda) = 1.45$ and $\tilde{n}_{TiO_2}(\lambda) = 2.44$, whereas for Si particles we make use of the internal materials library included in the software Lumerical Solutions. Regarding the MAPI film, we extract $\tilde{n}_p(\lambda)$ from ref [29], considering a model dielectric function that is fitted to the experimental reflectance and transmittance spectra according to the Forouhi–Bloomer formulation [30]. The latter enables us to retrieve broadband information with just a single simulation. Grain boundaries and morphology of the synthesized film is strongly dictated by the diversity of methods to prepare MAPI thin films resulting in a wide range of compounds with apparently similar composition but very different electrical and optical properties. The selected value of $\tilde{n}_p(\lambda)$ corresponds to the one for which highly performing perovskite devices are attained, and it that can be considered as an example of a standard in the field. This means that our results serve as a guide for identifying materials and range of parameters of the particle arrays that will yield large absorption enhancements. However, for different MAPI films, a full theoretical modeling considering the corresponding optical constants should be needed to find the optimum results. For the full cell configuration, we extract the complex refractive indexes of the fluorine-doped tin oxide (FTO), TiO_2 compact layer, spiro-OMeTAD, gold, and indium tin oxide (ITO) from ref [31]. The system is illuminated by a

Optics EXPRESS

plane wave (with $\lambda \in [400,800]$ nm) that propagates along the *z*-direction injected at the glass substrate. Perfectly matched layer (PML) absorbing boundaries are applied along the z-direction, and symmetry boundary conditions along the x and y directions. We analyze particle arrays in both square and hexagonal configurations. For square arrays, the size of the square simulation box along x and y directions define the array period p, while for hexagonal arrays, the size along one of the directions in the xy plane is set to be p, and the other one, $\sqrt{3}\cdot p$. Results are also compared to the outcome expected from disordered systems. In them, a uniform random particle distribution is created. The number of particles (N) per unit volume in this disordered system is set to be exactly the same as in the ordered system. Thus $N = V_b^r / V_b$, where V_b and V_b^r correspond to the volume of the MAPI film in the ordered and in the random case, respectively. Despite periodic boundary conditions are applied in the random distribution system, the simulation box extensions along the x and y directions (5x5 μ m^2) are sufficiently large so that array effects are minimized and can be ignored. Finally, to achieve converged and accurate results, a uniform mesh with a maximum mesh step of 5 nm spans the whole simulation box.

Following the definition in refs [21, 22], the integrated solar absorption enhancement, η, is given by:

$$\eta = \frac{\int_{400}^{780} A_{\mathrm{p}}(\lambda)\cdot \mathrm{AM1.5D}(\lambda)\,\mathrm{d}\lambda}{\int_{400}^{780} A_{\mathrm{Ref}}(\lambda)\cdot \mathrm{AM1.5D}(\lambda)\,\mathrm{d}\lambda}. \tag{1}$$

In the above equation, $A_p(\lambda)$ is the perovskite film absorptance with embedded particles, $A_{\mathrm{Ref}}(\lambda)$ is the perovskite absorptance of the same volume deprived of particles and taken as a reference, and $\mathrm{AM1.5D}(\lambda)$ is a standard for the solar radiance spectrum on the Earth surface assuming only direct sunlight illumination. Note that, in the case of complete solar cell configurations, we consider the perovskite absorptance contributing to the photocurrent, i.e., the absorptance of the MAPI film in addition to the absorptance of the porous TiO_2 scaffold fully infiltrated by perovskite. The integral wavelength range in Eq. (1) is taken according to the reported spectral values for which external quantum efficiencies is non-zero. For systems containing non-absorbing SiO_2 and TiO_2 particles, $A_{\mathrm{p}}(\lambda)$ is calculated through transmittance $T(\lambda)$ and reflectance $R(\lambda)$ calculations as

$$A_p(\lambda) = 1 - R(\lambda) - T(\lambda), \tag{2}$$

whereas for Si particles (with $k_{\mathrm{Si}} \neq 0$), perovskite and silicon absorptances are calculated independently using the Advanced method provided by Lumerical by taking:

$$A_j(\lambda) = \frac{1}{P_0}\left[\omega\varepsilon_0 \int \left|E(x,y,z,\omega)\right|^2 n_j(\omega)\, k_j(\omega)\, dV_j\right] \tag{3}$$

with P_0 being the incident power, ω the angular frequency, and E the normalized electric field vector. The integral is done over the corresponding perovskite or silicon volume, V_j. Moreover, in the full cell configuration, partial absorptance of each independent material is also calculated making use of Eq. (3), and the validity of the method is further proved by comparing the total absorptance of the system attained through Eq. (2), and that obtained by the summation of all partial absorptances.

Optics EXPRESS

3. Results and discussion

3.1 Square arrays of silica (SiO_2) and titania (TiO_2) particles embedded in thin MAPI films

Figure 2 shows FDTD calculations, as explained in the Methods section, of the solar spectrum weighted integrated absorptance enhancement, η, as a function of the array period p (spanning from 300 to 600 nm) for different particle radius r (ranging from 100 nm to 140 nm in a square arrangement). Figure 2(a) corresponds to SiO_2 particles, and Fig. 2(b) to TiO_2 ones. The normalized η value of a reference MAPI film of equal thickness without any particle inside, is displayed as a horizontal dashed line. All values above this reference ($\eta > 1$) speak of an improvement of the absorption in the MAPI film due to the incorporation of the particle array, while values below it ($\eta < 1$) represent a detriment of the optical absorption of the MAPI film. We find a maximum integrated absorption enhancement of 5.5% achieved for SiO_2 particles of $r = 140$ nm in a periodic square array of $p = 380$ nm. Remarkably, slight changes of the particle size and array period also lead to an improvement of η, making the system tolerant to deviations and hence suitable for experimental realization. In addition, for array periods $p \geq 600$ nm, no absorption enhancement occurs and the reference value is almost recovered ($\eta \approx 1$). On the other hand, inclusion of TiO_2 particles has a detrimental effect on the absorption of the MAPI film ($\eta < 1$). This material is the most commonly used as light scattering center for maximizing light absorption in dye sensitized solar cells [12,25], and it has been already proposed for improving light collection in PSC [13]. The reason for its poor performance in the case of perovskite films is the low refractive index contrast between the MAPI film and the TiO_2, which causes light to be not efficiently scattered by the spheres. For the optical constants herein considered, MAPI films without particles inside reach maximum solar spectrum weighted integrated absorption (SSWIA) for thicknesses above $\sim 1\mu m$, as it is shown in Fig. 3(a). However, we find that the inclusion of particle arrays do not lead to any improvement of the solar absorption for thickness larger than 500 nm, as scattering effects and high diffraction order resonances do not compensate for the amount of MAPI material removed by the presence of the particles. As an example, the analysis of the effect of a square array of SiO_2 particles integrated in a 500 nm thick MAPI film is also presented in Fig. 3(b). All spectra remain under the reference MAPI film, thus providing $\eta < 1$.

In what follows, we will analyze the absorptance spectra of the systems in Fig. 2 to find out the origin of absorption improvements or diminishments. The absorptance spectrum of the optimum system found in Fig. 2(a) (i.e., SiO_2 particles of $r = 140$ nm, and $p = 380$ nm (red colour line)) is shown in Fig. 4(a). Results for the same particle size but arranged with different lattice parameters are also shown in Fig. 4(a). We select $p = 340$ nm (blue line) and $p = 410$ nm (yellow line) as representative systems of spectra displaying distinct resonant features. Clear resonances are found near the wavelength at which collective effects should occur, i.e., $\lambda_R = \tilde{n}_j(\lambda) \cdot p / \sqrt{l^2 + m^2}$ with l and m being integers, and $\tilde{n}_j(\lambda)$ the refractive index of the glass substrate or the MAPI film. In particular, sharp resonances corresponding to the second diffraction order, i.e., $(l, m) = (1,1)$, taking $\widetilde{n_p}(\lambda) \approx 2.4$ as the perovskite refractive index, are noticed at $\lambda_R \approx 580$ nm, $\lambda_R \approx 650$ nm, and $\lambda_R \approx 700$ nm for lattice periods of $p = 340$

Optics EXPRESS

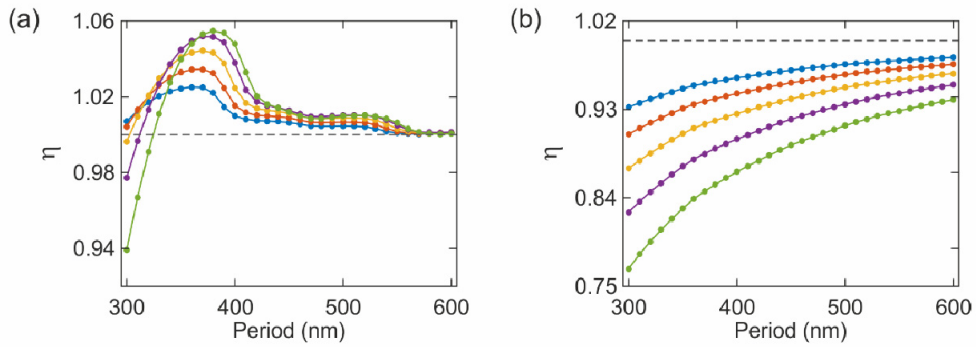

Fig. 2. (a-b) Integrated solar absorption enhancement, η, for MAPI films of $h = 300$ nm thickness, as a function of the period, p, for SiO_2 (a) and TiO_2 (b) particles of radius $r = 100$ nm (blue), $r = 110$ nm (red), $r = 120$ nm (yellow), $r = 130$ nm (purple) and $r = 140$ nm (green) in square lattice arrangements.

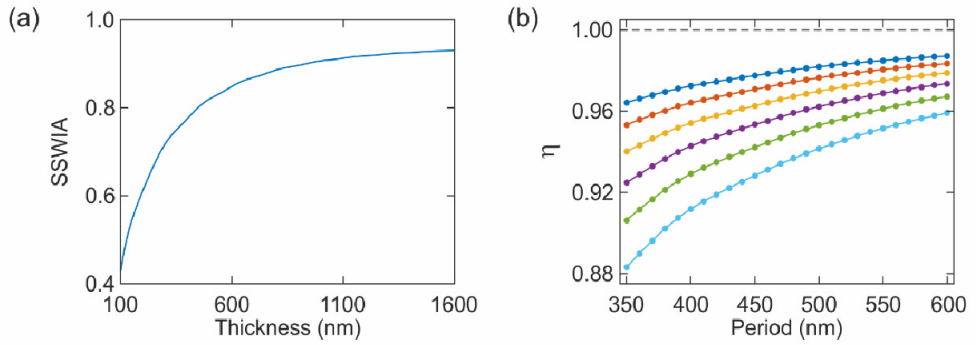

Fig. 3. (a) Solar spectrum weighted integrated absorptance (SSWIA) versus MAPI film thickness. (b) Integrated solar absorption enhancement, η, for MAPI films of $h = 500$ nm thickness, as a function of the period, p, for SiO_2 particles of radius $r = 120$ nm (blue), $r = 130$ nm (red), $r = 140$ nm (yellow), $r = 150$ nm (purple), $r = 160$ nm (green) and $r = 170$ nm (cyan) in square lattice arrangements.

nm, $p = 380$ nm, and $p = 410$ nm, accordingly. In addition to these resonant effects, broader absorption enhancements are also found at longer wavelengths. Note that they do not correspond to the first diffraction order since those lay out of the spectral range here considered. As we will show later, analysis of the electric field distribution in Fig. 5 provides further insight into their physical origin. In analogy with the optimum system, the outcome of a film containing a random distribution of the same particle size at the same concentration of $ff = 26\%$ (green dash line), is shown in Fig. 4(a) together with results of a reference MAPI film without any particle inside (black dash line). The comparison of ordered versus disordered systems demonstrates that only particle arrangements yield a better performance of the reference MAPI film. This is important to note, since many of the optical designs for optimizing light absorption in other type of solution processed solar cells incorporating SiO_2 or TiO_2 particles have considered a random distribution into the active layer [12, 25]. The case of hybrid perovskites is different, as they are already highly absorbing materials. For instance, it has been shown that no collective resonance can be excited when gold nanoparticles are directly embedded into the MAPI film, as the two absorbing materials do not allow the generation of a collective mode [21, 22].

Optics EXPRESS

Figure 4(b) shows the absorptance spectra of the same 300 nm MAPI film containing SiO_2 particles of $r = 100$ nm (purple line), $r = 120$ nm (green line), and $r = 140$ nm (yellow line) radius in a square array of $p = 410$ nm. As expected, the spectral location of λ_R remains unaltered when the particle size is varied (although the resonance intensity increases with the particle radius due to light scattering), whereas the resonance at long wavelengths changes position not only with the array period and particle size, but also with the film thickness, demonstrating its strong hybrid character. It is evident that despite all the systems present collective and/or hybrid resonances, only those with broad and intense resonances at proper wavelengths (i.e., $\lambda < 780$ nm, otherwise they do not contribute to the integrated solar absorptance) lead to a clear increment of the solar absorption. For large array periods ($p > 450$ nm), only third and higher diffraction orders (which are less intense) fall within the spectral range of study, yielding low η values (as shown in Fig. 2(a)).

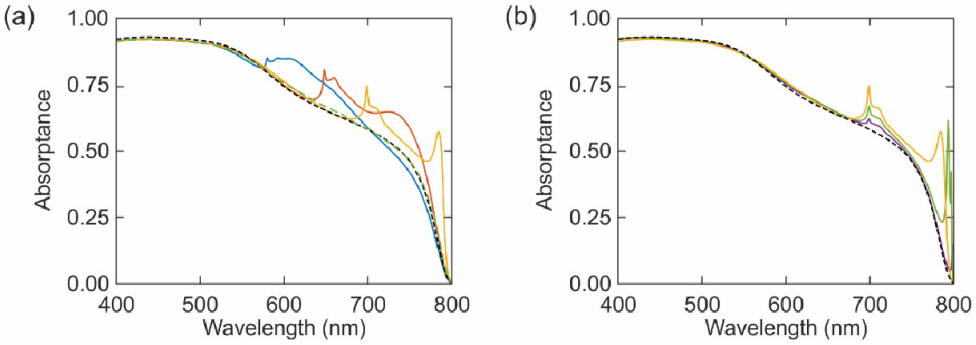

Fig. 4. (a) Perovskite absorptance spectra of a reference bared MAPI film of $h = 300$ nm thickness (black dash line), and of the same film containing SiO_2 particles of radius $r = 140$ nm arranged in a square lattice of $p = 340$ nm (blue line), $p = 380$ nm (red line) or $p = 410$ nm (yellow line). Results for a MAPI film of the same thickness and containing disordered particles of equal radius with a concentration of $ff = 26\%$ (equivalent to the concentration of an array with $p = 380$ nm) are draw with a green dash line. (b) Perovskite absorptance spectra of a MAPI film containing SiO_2 particles of radius $r = 100$ nm (purple line), $r = 120$ nm (green line), and $r = 140$ nm (yellow line) arranged in a square lattice of $p = 410$ nm.

A deeper analysis of the resonant features emerging in the absorptance spectra is presented in Fig. 5. Top panels show the electric field distribution $|E(x, y, z, \omega)|^2$ of the optimum system attained in Fig. 2(a) (whose spectrum is shown in Fig. 4(a) (red color)). At shortest resonant wavelengths ($\lambda_1 = 699$ nm, and $\lambda_2 = 710$ nm), an extended collective mode is observed at the substrate interface, while the field profile at longer wavelengths ($\lambda_3 = 784$ nm) shows a resonance emerging within the sphere and the appearance of a guided mode of hybrid nature (as the resonant wavelength changes with the film thickness). We would like to mention that sharp hybrid resonances with electric field intensities 50 times larger than those at λ_R, might be found for smaller particle size (results not shown here), but they do not contribute to η as they emerge at $\lambda > 780$ nm, and therefore, are excluded in the integral. Even if they could be considered, they are too narrow spectrally as to have a real impact on η. Bottom panels in Fig. 5 show the corresponding absorbed power (per unit volume) profiles displaying the spatial distribution where maximum absorption in the MAPI film occurs. Hexagonal arrays of SiO_2 particles embedded in thin MAPI films are also analysed in

Optics EXPRESS

Fig. 6. We find that a hexagonal pattern yields a very similar result to the square organization, getting a maximum η value of around 1.05 for SiO_2 particles of $r = 140$ nm with a lattice constant of $p = 440$. From a practical perspective, it should be considered that the typical SiO_2 particle arrangement attained when a suspension is deposited on a flat substrate is the hexagonal close packing [32]. Unfortunately, this arrangement (that could correspond to array periods of $p \approx 300$ nm), does not lead to an improvement of the absorption in the MAPI film. This means that, with any of the two canonical configurations herein considered, absorption enhancement of the MAPI film could be obtained only for periods significantly larger than the particle diameter, which implies the use of either a patterned substrate [33] or a sacrificial medium [34].

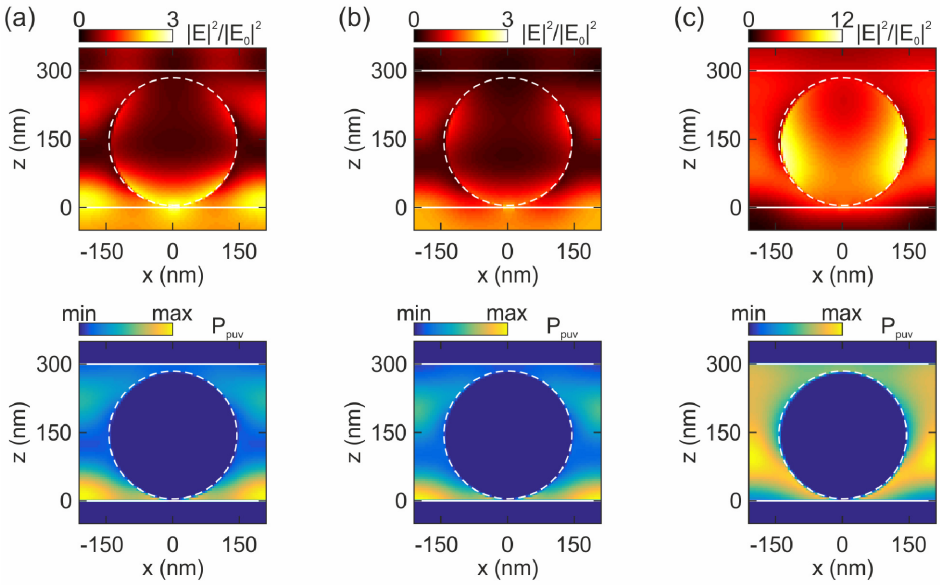

Fig. 5. Top panels show the electric field distribution $|E(x, y, z, \omega)|^2$ of a unit cell of a $h = 300$ nm thickness MAPI film containing SiO_2 particles of $r = 140$ nm arranged in a square lattice of $p = 410$ nm at the resonant wavelengths $\lambda_1 = 699$ nm (a), $\lambda_2 = 710$ nm (b) and $\lambda_3 = 784$ nm (c). Bottom panels display corresponding results of the absorbed power per unit volume at the same wavelengths. White lines are used to guide the eye distinguishing amongst different materials (substrate ($z < 0$ nm), cover ($z > 300$ nm), MAPI film (0 nm $\leq z \leq 300$ nm), and particle).

Optics EXPRESS

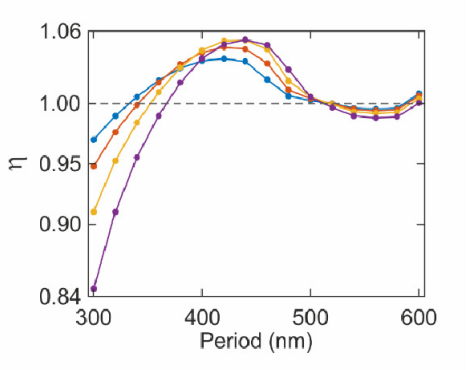

Fig. 6. Integrated solar absorption enhancement, η, for MAPI films of $h = 300$ nm thickness, as a function of the period, p, for SiO_2 particles of radius $r = 110$ nm (blue), $r = 120$ nm (red), $r = 130$ nm (yellow), and $r = 140$ nm (purple) in hexagonal lattice arrangements

3.2 Silicon (Si) particles embedded in thin MAPI films

We also analysed the effect of including submicrometric Si spheres [23, 24] into the MAPI film. Previous approaches have considered the incorporation of Si nanocrystals in solid matrices in both photovoltaic and light emitting devices to increase the efficiency of charge extraction and transport [35, 36]. Solution processed films, as it is the case of perovskites, should in principle allow the embedding of submicron size Si particles either randomly distributed or arranged in a lattice. Figure 7(a) shows η as a function of the lattice period p for Si particles of radius ranging from 80 to 120 nm arranged in a square array. We find that a maximum value of $\eta = 1.1$ is achieved for Si particles of $r = 100$ nm and array period of $p = 320$ nm. Figure 7(b) shows the perovskite (red line) and Si (blue line) absorptance spectra of the optimum system obtained in panel a. In addition, the result of a bare reference MAPI film (black dash line) is also outlined in panel b. In it, we can identify a second order diffraction resonance emerging at wavelength $\lambda_R = 546$ nm, and other resonances emerging at $\lambda = 640$ nm, and $\lambda = 773$ nm. Interestingly, a double contribution of near field (with high field enhancement around the particle) and far field (related to light scattering) effects occur at all resonant wavelengths, similarly to what happens with metallic particles in MAPI films [21, 22]. However, Si absorbs light in such a way that collective modes can still be built up leading to sharp resonances that blur and widen when they hybridize with localized resonances of the particles. That effect results in broad resonances that effectively contribute to the MAPI absorptance at appropriate wavelengths at which maximum number of solar photons are captured. The latter can be seen in Fig. 8 by examining the electric field distribution $\left|E(x,y,z,\omega)\right|^2$ (top panels) and the absorbed power per unit volume (bottom panels) at the resonant wavelengths ($\lambda_1 = 546$ nm (a), $\lambda_2 = 640$ nm (b) and $\lambda_3 = 773$ nm (c)). Therefore, in contrast to the results attained for SiO_2 and TiO_2 particles, it is expected that random distribution of Si particles embedded in MAPI films will also lead to an enhancement of the solar absorption since the contributing modes are of localized nature. Actually, it has been recently demonstrated that the use of low-loss high-refractive-index silicon nanoparticles randomly distributed within the perovskite film improves the optical properties of organo-metallic perovskite films and metasurfaces yielding a strong enhancement of photoluminescence as well as useful light absorption in structured MAPI films [37]. Those results demonstrate that our approach can be further extended and combined with structured perovskite films.

Optics EXPRESS

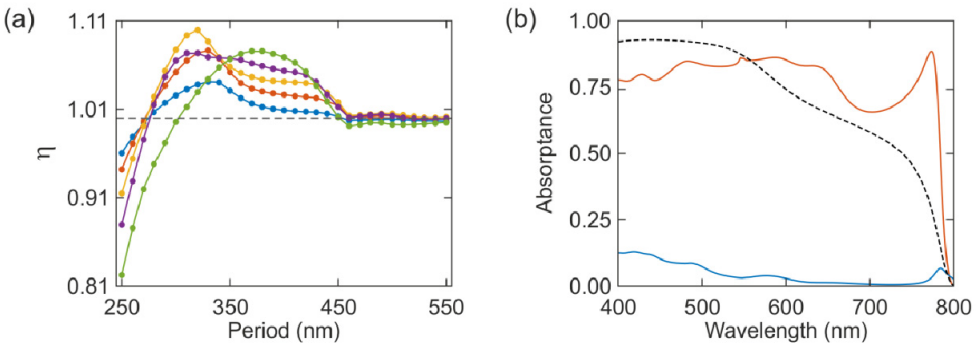

Fig. 7. (a) Integrated solar absorption enhancement, η, for MAPI films of $h = 300$ nm thickness as a function of the period, p, for Si particles of radius $r = 80$ nm (blue), $r = 90$ nm (red), $r = 100$ nm (yellow), $r = 110$ nm (purple), and $r = 120$ nm (green) in square lattice arrangements. (b) Absorptance spectra of a reference MAPI film (black dash line) without any particle inside, and that of the optimum system attained in panel (a), i.e., a MAPI film containing Si particles of radius $r = 100$ nm arranged in an array with $p = 300$ nm. Red line corresponds to the MAPI film, and blue line to the Si absorptance.

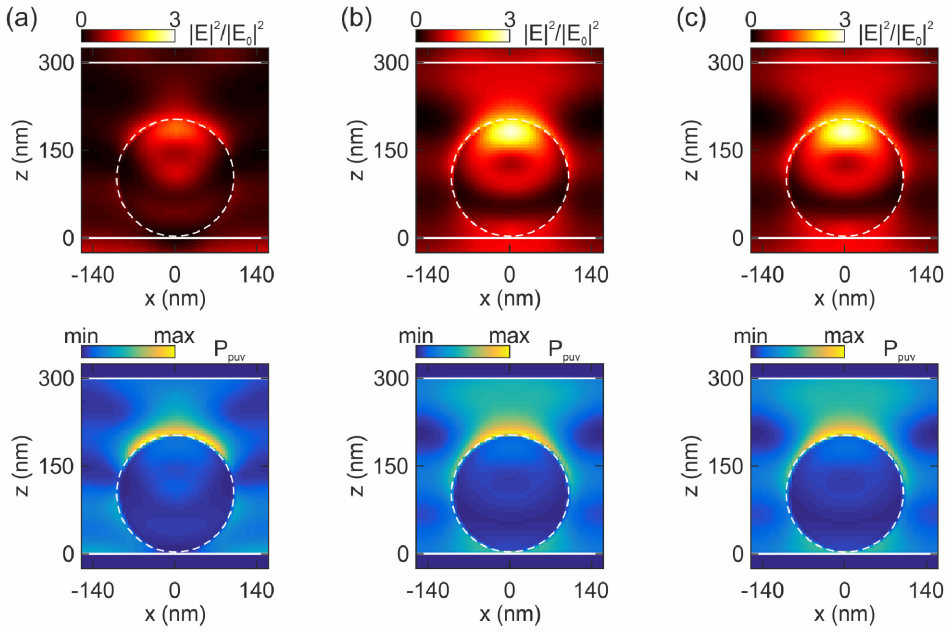

Fig. 8. Electric field distribution $|E(x, y, z, \omega)|^2$, top panels, of a unit cell of a $h = 300$ nm thickness MAPI film containing Si particles of $r = 100$ nm arranged in a square lattice of $p = 320$ nm at the resonant wavelengths $\lambda_1 = 546$ nm (a), $\lambda_2 = 640$ nm (b) and $\lambda_3 = 773$ nm (c). Bottom panels display corresponding results of the absorbed power per unit volume at the same wavelengths. White lines are used to guide the eye distinguishing amongst different materials (substrate, cover, MAPI film, and particle).

Optics EXPRESS

3.3 Silicon (Si) particles embedded in standard and semi-transparent perovskite solar cells

Finally, we theoretically evaluate the effect of incorporating Si particles in standard opaque (with a gold contact) and semi-transparent (with an ITO contact) solar cells. We consider a representative configuration as described in Fig. 1(b), with a multilayer configuration. It consists on a semi-infinite glass substrate, followed by FTO (500 nm), a TiO_2 compact layer (10 nm), a 50% porous TiO_2 scaffold fully infiltrated with perovskite (100 nm), a perovskite capping layer with an array of particles at the bottom surface (300 nm), spiro-OMeTAD (80 nm), and 80 nm of gold contact (for the standard cell) or 100 nm of ITO contact (for the semi-transparent cell). We evaluate particle spheres of radius spanning from 80 to 140 nm, in lattice parameters ranging from 250 to 550 nm. Note that the optimum system might be slightly different to the one attained in the simple MAPI film arrangement since the incorporation of the 100 nm TiO_2 scaffold infiltrated with perovskite might be seen as a new system in which the particle position along the z-direction, inside an "effective" 400 nm perovskite film, is modified (i.e., both the film thickness and the particle location are modified, which has a strong impact on the perovskite absorptance) [21]. Figure 9(a) shows η as a function of p for Si particles arranged in a square configuration inside an opaque solar cell. Figure 9(b) shows the same calculations for semi-transparent solar cells. For each cell, a different optimum configuration is obtained, as light is differently reflected back by the contact and thus, the optical response is strongly modified. We find that it is possible to enhance the integrated solar absorptance up to 3.4% in the opaque cell with Si particles of 100 nm radius and $p = 320$ nm, and up to 10% in a semi-transparent cell with particles of 130 nm radius and $p = 370$ nm. Partial parasitic and productive absorptances of all materials composing the optimum system in the semi-transparent configuration are shown in Fig. 9. For comparison, the absorptance of a MAPI film inside a reference cell (without particles) is also shown. It is interesting to note that the cell containing the particle array absorbs less efficiently in the blue part of the visible spectrum than the reference cell, but it is highly compensated by the absorptance in the red part of the spectrum at which the number of solar photons is maximum. The localized nature of the resonances emerging in the red part of the spectrum as it is shown in Fig. 10, indicates that improvement of light absorption in perovskite films containing a random distribution of Si particles is possible.

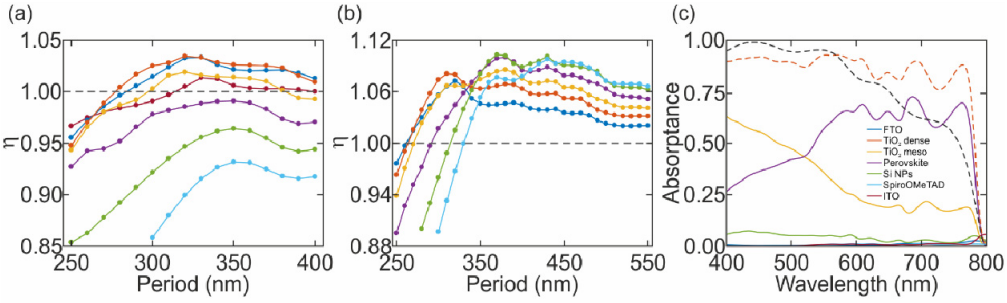

Fig. 9. (a) Integrated solar absorption enhancement, η, for an opaque solar cell (having an 80 nm gold contact) as in the configuration described in Fig. 1(b), as a function of the period, p, for Si particles of radius $r = 80$ nm (garnet), $r = 90$ nm (blue), $r = 100$ nm (red), $r = 110$ nm (yellow), $r = 120$ nm (purple), $r = 130$ nm (green) and $r = 140$ nm (cyan) in square lattice arrangements. (b) Same calculations as in panel (a) but in a semi-transparent solar cell (having a 100 nm ITO contact). (c) Productive absorptance spectra of a MAPI film embedding an optimized design of Si particles (red dashed line) of radius $r = 130$ nm arranged in an array with $p = 370$ nm. Partial absorptances of all materials are shown according to the colors indicated in the figure. For the sake of comparison, the absorptance of a MAPI film of similar thickness without any particle inside (black dashed line) is also shown.

Optics EXPRESS

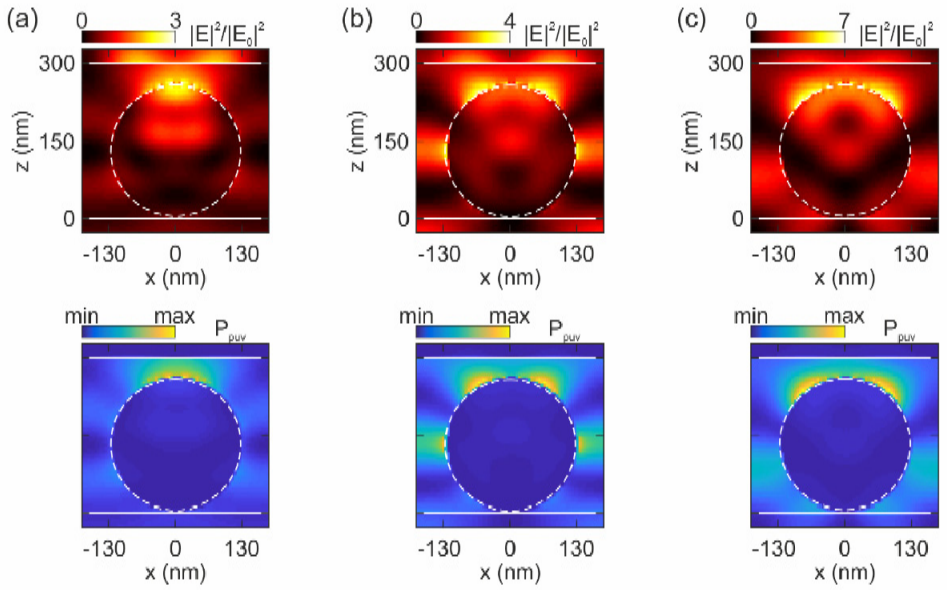

Fig. 10. Electric field distribution $|E(x,y,z,\omega)|^2$, top panels, of a unit cell of a $h = 300$ nm thickness MAPI film containing Si particles of $r = 130$ nm and $p = 370$ nm at the localized resonances emerging at long wavelengths $\lambda = 609$ nm (a), $\lambda = 686$ nm (b), and $\lambda = 763$ nm (c). Bottom panels display corresponding results of the absorbed power per unit volume.

4. Conclusions

We have developed a deep theoretical analysis of the solar absorption enhancement of MAPI films in which arrays of dielectric particles are incorporated. The effect of realistic materials has been considered. Both opaque and semitransparent solar cell configurations have been analysed, light harvesting improvements being attained in both cases. We have found sets of parameters yielding solar absorption enhancements of around 6% and 10% with SiO_2 and Si particles, respectively, arranged in square arrays. Conversely, TiO_2 particles cannot enhance light harvesting in any of the tested configuration. Analysis of absorptance spectra demonstrates that the excitation of collective and hybrid (of both localized and propagating character) resonances are at the heart of the attained absorption enhancements. Contrarily to what happens with SiO_2 particles, we have pointed out that random distribution of Si particles embedded in MAPI films should give rise to high solar absorption enhancements since localized resonances dominate the contribution. Finally, we have tested the incorporation of Si particle arrays in standard opaque solar cells and in semi-transparent cells, finding that it is possible to attain solar absorption enhancements in both cases. The improvement expected for semitransparent cells incorporating Si particles (around 10%) may lead to their integration in the flowering tandem solar cell technology. With the aim of minimizing the environmental impact of the use of perovskite-based solar cells, approaches considering other perovskite compositions have been proposed. The concepts here considered to maximize light absorption by embedding dielectric particles can be extended to other perovskites following the ABX_3 formula, being A an organic cation, B a metal cation, and X a halide anion. In this sense, a fine tuning of the particle array (concerning particle size and array period) should be analyzed for other halide perovskite materials, as their bandgap might be different from the one here considered, and the contribution of localized and collective resonances to maximize light absorption should be spectrally adjusted. Furthermore, new tests should be developed for all particle materials (TiO_2, SiO_2, and Si) since the refractive index contrast between the particles

Optics EXPRESS

and the perovskite films can lead to much different scattering effects, thus affecting to the contribution of near and far field effects. As an aside, we note that the solar cells operation also relies on other parameters too such as carrier transporting from absorbers to electrodes, ion-migration and temperature increase due to the high field enhancements attained. Despite a full analysis of the previous aspects should be performed, we might say that considering that long-ranged charge carrier diffusion has been reported in efficient MAPI films reaching up to 65 μm in the case of single crystals and 10 μm in nanocrystalline thin films, respectively [38–41], and that the thickness of the perovskite films we consider in this work is always below 600 nm, there is no reason to believe that the deviation of the optical absorption (i.e., charge generation) profile from the canonical Lambert-Beer curve to a more complex one caused by the presence of particles will alter the collection efficiency of the device. Ion migration might be affected by the presence of dielectric particles because it implies that part of the volume might not be available, in principle, for charge (electronic or ionic) transport. This phenomenon is one of the most intriguing and debated in the field even for homogeneous films [42], so a deep understanding of this matter for the case of nanoparticle doped films like the ones we propose should be the subject of further research. We expect that the operation of the solar devices embedding dielectric particles that we propose here will not be affected by the temperature increment associated to high field enhancements, also because perovskite solar cells can operate efficiently within a relatively wide temperature range [43]. Finally, our work complements recent efforts on the analysis of the effect of metal particles that give rise to enhancement effects based on plasmonic resonances and offer an alternative route when the integration of metals is not possible.

Funding

European Research Council under the European Union's Seventh Framework Programme (FP7/ 2007–2013)/ERC Grant Agreement no. 307081 (POLIGHT) and the Spanish Ministry of Economy and Competitiveness under grant MAT2014-54852-R and MAT2017-88584-R, is gratefully acknowledged. A.J.-S. acknowledges the Spanish Ministry of Economy and Competitiveness for funding through an FPI program under the project MAT2011-23593, and S.C.-P. for funding through a Juan de la Cierva – Incorporación under grant IJCI-2016-28549.